Exploring the influence of wind stress and ocean stratification on sea surface temperature variability in the central tropical Pacific

by

Gian Luca Eusebi Borzelli(1*), Cosimo Enrico Carniel(2), Sandro Carniel(3), Mauro Sclavo(3)

[1]Center for Remote Sensing of the Earth (CeRSE), Rome Italy. e-mail: luca_borzelli@yahoo.it; gianluca.borzelli@cerse.it

[2]Institute for Atmospheric and Climate Sciences, ETH Zürich, Zurich, Switzerland.

[3]CNR, Istituto di Scienze Polari, Venezia Italy.

*Corresponding author

Abstract.

The El Niño-Southern Oscillation (ENSO) is a climate oscillation in the tropical Pacific sustained by a positive feedback between sea surface temperature (SST) gradient and the Walker circulation, known as the Bjerknes feedback. This results in an oscillation in the SST anomaly between warm (El Niño) and cold (La Niña) phases. In traditional ENSO theories, the Bjerknes feedback amplifies an initial disturbance to produce a full El Niño or La Niña, while the Sverdrup transport, caused by off-equatorial wind stress (WS) curl, determines the slow charging of the equatorial Pacific through deepening of the thermocline. However, recent research has emphasized the role played by the WS divergence in generating Kelvin waves that initiate El Niño. To account for changes in the action of the WS over a varying ocean stratification, we introduce a dimensionless WS (DWS) and use the Helmholtz decomposition to break it down into an irrotational (curl-free) and solenoidal (divergence-free) component to study ENSO variability over the interannual-to-interdecadal time scale. We show that the irrotational component of the DWS drives the thermocline dynamics on interannual time-scales, while the solenoidal component, which drives Sverdrup transport, determines off-equatorial internal waves, referred to as q-waves, that induce changes in the thermocline depth over longer time-scales. Furthermore, we develop an integral relation that links the variability of the thermocline depth anomaly across the tropical Pacific to the Niño-3.4 index variability. We conclude that the DWS irrotational component determines the Niño-3.4 index interannual variability, while the solenoidal component determines its long-term variability.

1. Introduction

Since the 17th century, Peruvian fishermen have observed a recurring anomalously warm current along the Peruvian coast near Christmas. They named this phenomenon "El Niño" (the little boy) or "Niño de Cristo" (Christ child). The first scientific mention of "El Niño" dates back to the early 1890s (Carrillo, 1892). However, until the first half of the 20th century, it was believed to be a local occurrence limited to the coasts of Peru and Ecuador. Since then, significant discoveries have been made about the structure and time-space scales involved in El Niño. It is now understood to be a manifestation of the strongest year-to-year climate fluctuation on our planet known as El Niño Southern Oscillation (ENSO). A crucial aspect of the ENSO cycle is the positive feedback relationship between the zonal sea surface temperature (SST) gradient and the Walker circulation, referred to as the Bjerknes feedback (e.g., Bjerknes, 1969; Wyrtki, 1975). The surface easterly winds of the Walker circulation cause the thermocline to sink in the west and rise in the east, resulting in the formation of the western warm pool and the upwelling cold tongue in the eastern part of the basin. This zonal SST gradient further reinforces the easterly winds. El Niño and La Niña are extreme events that occur when the Walker circulation weakens (El Niño) or strengthens (La Niña), leading to a decrease or increase in upwelling in the eastern tropical Pacific. This process results in an irregular oscillation between warm (El Niño) and cold (La Niña) phases, with peaks occurring in boreal winter and recurring every 2-5 years (Rasmusson et al., 1990; Jiang et al., 1995).

Our understanding of the oscillatory nature of ENSO relies on recognizing the relationship between changes in internal ocean dynamics and changes in the wind stress pattern. By interpreting the tropical Pacific Ocean as a double-layer system, the heat stored in the water column depends on the depth of the interface that separates the surface and bottom layers. The zonal deformation of this interface (i.e. the dynamical ocean subsurface memory) is sustained by the dynamical balance between the fluid internal zonal pressure gradient and zonal winds (Cane and Zebiak, 1985; Philander, 1990; Jin, 1997; Burgers et al., 2005; Jin et al., 2006).

Therefore, the SST anomaly, depth of the interface separating the surface and bottom layers, whose fluctuations from a reference depth are often assumed to coincide with fluctuations in the depth of a sentinel isotherm (typically the 15 °C, 17 °C, or 20 °C isotherm depth referred to as Z_{15}, Z_{17}, Z_{20}), and zonal wind stress are a natural set of “state variables” that can be used to infer the basic physics underlying ENSO. In a broad sense, and assuming that over the interannual time-scale the tropical Pacific climate system can be approximated by a linear system, the dynamics underlying ENSO is described by linear or non linear models that relate the evolution of the state variables to each other (Penland and Sardeshmukh, 1995; Newman et al., 2009; Newman et al., 2011; Capotondi and Sardeshmukh, 2015).

https://doi.org/10.5194/egusphere-2026-2393
Preprint. Discussion started: 28 May 2026

Over the past 25 years, the linear recharge/discharge oscillator (LRDO) model, proposed by Jin (1997), Burgers et al. (2005), and Jin et al. (2006), has served as a robust conceptual framework for interpreting the interannual variability of SST anomalies in the tropical Pacific, despite some discrepancies with observations. In this model, wind stress curl plays a fundamental role in the preconditioning and evolution of ENSO. During the recharge phase, easterly wind (EW) anomalies generate off-equatorial anticyclonic wind stress curls, resulting in a net equatorward Sverdrup transport that deepens the equatorial thermocline. Conversely, during the discharge phase, westerly wind (WW) anomalies produce off-equatorial cyclonic wind stress curls, causing a poleward Sverdrup transport that moves warm water away from the equator and shallows the equatorial thermocline. The recharge/discharge model describes ENSO as a self-sustained cycle driven by the slow buildup and drainage of warm water towards and from the equator. From a mathematical perspective, the ocean is represented as a two-layer system, in which the deepening of the interface between the layers represents the charging phase, while the shoaling of this interface represents the discharge. In the original formulation (Jin, 1997), the thermocline variability is separated into two components: the zonal tilt (i.e. the difference in thermocline depth between the east and west), which responds quickly to winds, and the mean equatorial heat content (the average depth of the thermocline across the entire equator), which changes slowly through Sverdrup transport. The "oscillation" is related to the lag between these two components. The zonal wind stress immediately affects the tilt, but it takes time for the Sverdrup transport to change the mean depth of the thermocline (the recharge/discharge).

The Bjerknes feedback is represented in the recharge/discharge model as a growth mechanism that turns an initial disturbance in to a full El Niño or La Niña event. While Sverdrup transport determines the slow charging of the equatorial Pacific providing the "memory" (i.e. the mean depth of the equatorial thermocline) of the equatorial Pacific climate system, the Bjerknes feedback amplifies an initial disturbance into a full El Niño or La Niña event. In this study, we discuss the relationship between changes in the wind stress curl and divergence, and tilting of the thermocline to explain ENSO variability over the interannual-to-interdecadal time scale.

Other studies have emphasized the importance of equatorial Kelvin waves (KWs) forced by westerly wind (WW) events. Picaut and Delcroix (1995) investigated equatorial wave sequences during the 1986–1987 El Niño and showed that anomalous zonal advection was closely associated with KWs excited by a succession of local WW events in the western and central tropical Pacific. These findings underscore the central role of WWs in triggering SST anomalies on interannual timescales (see also Wang and Fiedler, 2006; Santoso et al., 2017).

More recently, Eusebi Borzelli and Carniel (2023) examined the zonal displacements of the convergence region between westerly and easterly winds (EWs). They demonstrated that internal KWs are systematically generated beneath the WW/EW convergence zone and that the zonal position of this convergence is highly correlated with the Southern Oscillation Index (SOI). In their terminology, the WW/EW convergence corresponds to the region of minimum wind stress divergence (i.e., the maximum absolute value of wind stress divergence), emphasizing the critical role of wind stress divergence in controlling interannual SST anomaly variability.

Overall, these studies indicate that both wind stress curl and wind stress divergence are key dynamical factors governing the initiation and evolution of El Niño events.

Over the long term, time series of ENSO indexes exhibit a ‘‘regime shift’’ from 1976, first noted by Quinn and Neal (1984, 1985). Subsequent studies (Trenberth, 1990; Trenberth and Hurrell, 1994; Graham, 1994), have emphasized the importance of this feature in relation to interdecadal climate variability over the North Pacific. Since then, several studies have concentrated on the interdecadal or longer ENSO variability. In this context, it is important to note that the behavior and characteristics of ENSO are closely linked to the slowly changing background mean climate conditions of the equatorial Pacific. These conditions impact ENSO initiation and growing (Fedorov and Philander, 2001; An et al., 2008; Collins et al., 2010). It is projected that the mean climate state of the tropical Pacific will change due to global warming, with a faster rate of warming in the equatorial Pacific compared to off-equatorial regions (Liu et al., 2005; Collins et al., 2010). This warming is expected to be more pronounced in the eastern and western equatorial Pacific compared to the central region (Xie et al., 2010). Additionally, the surface of the ocean is expected to warm more quickly than the subsurface (An et al., 2008). This surface warming pattern is responsible for an increase in rainfall, particularly in the eastern part of the basin, which is a defining characteristic of extreme El Niño events (Zhong et al., 2025). Accordingly, Cai et al. (2015; 2022) observed that El Niño events are becoming more frequent and intense under global warming.

From a slightly different perspective, some research has focused on the effect of meridional mean-state change on low frequency variability of El Niño. It is well known that the intertropical convergence zone (ITCZ) is typically located north of the equator for most of the year, resulting in climatological cross-equatorial southerly winds across the eastern equatorial Pacific. The relaxation of these southerly winds crossing the equator leads to a weakening of the cold and westward currents south of the equator, contributing to the thermocline downwelling and SST warming in the eastern equatorial Pacific, which in turn modulates El Niño intensity (Philander and Pacanowski, 1981; Périgaud et al., 1997; Hu and Fedorov, 2018; Peng et al., 2020). This observation has led some authors to investigate ENSO variability

https://doi.org/10.5194/egusphere-2026-2393
Preprint. Discussion started: 28 May 2026

over interdecadal or longer time scales in relation to low frequency variability of the ITCZ and meridional cross-equatorial southerly winds (Xie et al., 2018; Capotondi and Ricciardulli, 2021; Wang and Zheng, 2023).

Here, to account for the modulation of wind stress forcing caused by the slowly varying surface density and related changes in the reduced gravity (g'), we introduce a dimensionless wind stress (DWS). The DWS is defined as the ratio between the wind stress and the product of the surface-layer density and the square of the first baroclinic mode velocity. The first baroclinic mode velocity, denoted by c_1, is given by $(g'H)^{1/2}$, where H is the depth of the surface layer and g' is the reduced gravity (see appendix B for details).

To investigate the relative contributions of DWS curl and divergence to SST anomaly variability in the tropical Pacific on interannual to interdecadal timescales, we decompose the DWS into irrotational (curl-free) and solenoidal (divergence-free) components using the Helmholtz decomposition. Assuming the tropical Pacific as a two-layer ocean, we follow Capotondi and Sardeshmukh (2015) and use variations in Z_{15} as a proxy for fluctuations in the depth of the interface layer. This allows us to derive an integral relationship linking basin-wide changes in the Z_{15} anomaly to the Niño-3.4 index (N_{34}). The N_{34} is defined as the five-month median-filtered mean SST anomaly over the region 5°S–5°N, 190°E–240°E (the Niño-3.4 region). Our results indicate that interannual variability in N_{34} is primarily driven by the coupling between the irrotational component of the DWS and thermocline depth fluctuations. In addition, we find that differential temperature changes between the surface and subsurface ocean layers (An et al. 2008) induce variations in the reduced gravity field (g'), thereby modulating the background ocean dynamics. We show that the interaction between the solenoidal component of the DWS and these slow changes in ocean stratification provides a mechanistic explanation for the long-term modulation of El Niño intensity.

2. The data

Surface winds and SST were obtained from the Copernicus data archive. Copernicus provides parameters over a regular spatial grid of 0.25º×0.25º. This study utilized ERA5 monthly surface zonal winds and SST over the region 160ºE-270ºE, 20ºS-20ºN in the period Jan 1960-Dec 2020.

The wind stress was calculated from surface wind components using the standard formula $\boldsymbol{\tau}=\rho_{air}\cdot c_D\cdot(v_x^2+v_y^2)^{1/2}\cdot\boldsymbol{v}$, where $\boldsymbol{v}=(v_x, v_y)$ is the surface wind, ρ_{air} is the air density at the ocean surface (taken as 1.2 kg/m^3) and c_D is the drag coefficient (taken as $1.2\cdot10^{-3}$ if $(v_x^2+v_y^2)^{1/2}<11$ m/s and $[0.49+0.065\cdot(v_x^2+v_y^2)^{1/2}]\cdot10^{-3}$ if $(v_x^2+v_y^2)^{1/2} \geq 11$ m/s, for details see Large and Pond, 1981).

SST data were used to compute the N_{34}. Monthly SST data from January 1960 to December 2020, were extracted from the Copernicus database over the Niño-3.4 region. The SST anomaly was computed using as a reference climatological baseline, the period January 1991-December 2020.

The Institute of Atmospheric Physics (IAP) at the Chinese Academy of Sciences (CAS) has provided salinity and temperature (TS) data for the water column. These data consist of monthly objective maps covering the entire global ocean from January 1960 to December 2020, sampled over a regular spatial grid of 0.5°×0.5°. The data includes TS profiles from the surface to a depth of 2000 m (for more information, refer to Cheng et al. 2017). In this study, data from the region (160°E-270°E, 20°S-20°N) were extracted to compute the Z_{15} and seawater density profiles.

The velocity of the first baroclinic mode and the depth of the main thermocline were calculated using sea water density profiles, as described in Appendix B. It should be noted that the CAS-IAP data is sampled on a 0.5°×0.5° grid, while the Copernicus wind data is sampled on a 0.25°×0.25° grid. To calculate the DWS, we used a "nearest neighborhood" interpolation method to undersample the wind stress data.

3. The Z_{15}-N_{34} integral relationship

Our objective is to explain the variability of N_{34} by utilizing an integral relationship that connects the variability of the Z_{15} anomaly across the entire observation region (160°E-270°E, 20°S-20°N) to N_{34}. This relationship can be expressed as

$$N_{34}(t) = \int_{(S)} \frac{dx}{S} w(x) Z(x,t) = \sum_{m=1}^{M} Z\left(x_m, t\right) \cdot w\left(x_m\right) \tag{1}$$

In this equation $Z(x_m,t)$ represents the Z_{15} anomaly at point x_i on date t, and $N_{34}(t)$ represents the N_{34} on date t. The unknowns $w(x_m)$ define the linear model that links Z and N_{34}. We determine $w(x_m)$ by requiring that the representation (1) is “optimal” in the least-square sense, namely we require that the Root Mean Square (RMS) between N_{34} and its representation on the right-hand side of (1) is minimum, i.e.

$$min \left\{ \left\langle \left[N_{34}(t) - \sum_{m=1}^{M} Z\left(x_m; t\right) \cdot w\left(x_m\right) \right]^2 \right\rangle \right\}_{w(x_1), w(x_2), \ldots, w(x_M)} \tag{2}$$

where the bra-ket symbol denotes temporal averaging. By computing the derivative with respect to $w(x_k)$ of the RMS, and requiring the minimum condition, we obtain a system of linear equations for the unknowns $w(x_m)$ ($m=1...M$), i.e.

$$\sum_{m=1}^{M} A\,(x_k, x_m) \cdot w(x_m) = n(x_k) \tag{3}$$

where

$$\begin{aligned} n(x_k) &= \int_0^T \frac{dt}{T} N_{34}(t) \cdot Z(x_k, t) \\ A(x_k, x_m) &= \int_0^T \frac{dt}{T} Z(x_k, t) \cdot Z(x_m, t) \end{aligned} \tag{4}$$

The matrix $\boldsymbol{A}$, with elements $(\boldsymbol{A})_{km} = A(x_k,x_m)$, is the autocorrelation matrix of Z. Taking this in to account, denoting with λ_n the variance explained by n^th^ Empirical Orthogonal Function (EOF) of Z, with Y_n the n^th^ dimensionless EOF, and with α_n its corresponding dimensionless Principal Component (PC), we have (see Appendix A for the calculation)

$$w(x_m) = \sum_n \frac{c_n}{\sqrt{\lambda_n}} \cdot Y_n(x_m) \tag{5}$$

where the sum is extended to all EOFs of Z, and c_n is the projection of the N_{34} along the direction of the n^th^ PC, i.e.

$$c_m = \int_o^T \frac{dt}{T} \alpha_m(t) \cdot N_{34}(t) \tag{6}$$

Note that $w(x)$ is a transfer function that maps the Z_{15} anomaly over the entire tropical Pacific to the average SST anomaly over the central tropical Pacific. In Figure 1a, we show the measured N_{34} (blue solid line) and the N_{34} rebuilt from the Z_{15} anomaly using equation (1) and transfer function $w(x)$ given by equations (5) and (6). To rebuild the N_{34}, we have truncated the sum (5) to the first four EOFs, which cumulatively explain 84% of the overall Z_{15} data set variance. The two dashed lines represent the estimates of the transfer function obtained from the EOF analysis of the Z_{15} anomaly performed using data from the entire observation period (i.e. 1960-2020, red dashed line) and the sub-period 1960-1990 (green dashed line). In both cases, the N_{34} is accurately reconstructed, indicating the stability of the method in relation to the period over which the EOF analysis is performed. This is further supported by the similarity between the transfer functions estimated from the EOF analysis of the Z_{15} anomaly over

https://doi.org/10.5194/egusphere-2026-2393
Preprint. Discussion started: 28 May 2026

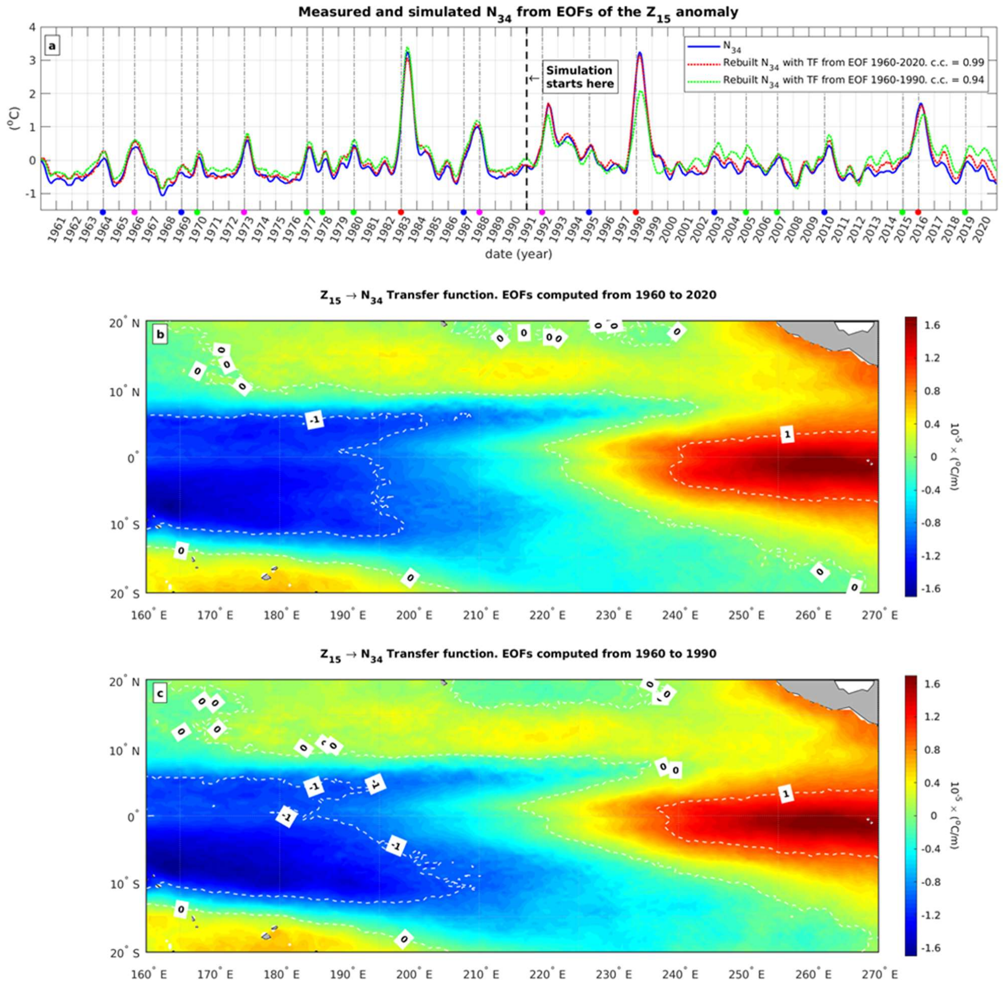

Figure 1: a) The blue solid line represents the measured N_{34} values, while the dashed lines represent the simulated N_{34} values from the first four EOFs of the Z_{15} anomaly. The red dashed line shows the N_{34} values simulated from the transfer function calculated using EOF analysis from 1960 to 2020, while the green dashed line shows the N_{34} values simulated from the transfer function calculated from EOF analysis from 1960 to 1990. Colored dots on the bottom horizontal axis represent El Niño events obtained from https://ggweather.com/enso/oni.htm. Color of the dots represent El Niño event intensity, with the following legend: red, extreme; magenta, strong; blue, moderate; green, weak. b) Z_{15} anomaly-N_{34} transfer function calculated from the first four EOFs of the Z_{15} over the period 1960-2020. c) Z_{15} anomaly-N_{34} transfer function calculated from the first four EOFs of the Z_{15} over the period 1960-1990.

the entire observation period and the period 1960-1990 (see Figures 1b and 1c). A general analysis of the transfer function's spatial structure indicates that it is characterized by values significantly different from zero in the region comprised approximately between 10°S and 10°N. This suggests that variations in the Z_{15} anomaly outside of this region have minimal impact on changes in the N_{34}. Within the region 10°S-

10ºN, the transfer function displays significantly positive values in the eastern part of the basin, notably negative values in the western, and values close to zero in the central area. This highlights a key geographical feature of the tropical Pacific climate system: the zonal tilting of the thermocline, which drives the atmospheric response related to the Bjerknes feedback. In the eastern Pacific, the thermocline is shallow and upwelling is strong, so even small vertical movements of the Z_{15} determine changes in the SST. In the western Pacific, the thermocline is deep, and its variations are critical for generating eastward propagating KWs. On the other hand, the central Pacific acts as a buffer zone where the thermocline is at an intermediate depth. In this region, there is no upwelling, and even a large vertical shift in the Z_{15} anomaly does not necessarily result in SST changes.

4. Wind stress and Z_{15}: "quasi-balance" and residual mean dynamics

We start with the full double layer, linearized shallow water equations, in which the term $\boldsymbol{\tau}/(g'\cdot H\cdot\rho)=\boldsymbol{\tau}/(c_1^2\cdot\rho)$ is expressed as the sum of a solenoidal (i.e. divergence-free) and irrotational (curl-free) vector field, as prescribed by the Helmholtz decomposition (see e.g Morse and Feshbach 1953), i.e.

$$\frac{\boldsymbol{\tau}}{g'\cdot H\cdot\rho}=\frac{\boldsymbol{\tau}}{{c_1}^2\cdot\rho}=\nabla\phi+\nabla\times\boldsymbol{A} \tag{7}$$

In equation (7), $\boldsymbol{\tau}$ represents the wind stress, g' the reduced gravity, H and ρ the thickness and density of the surface layer, and $c_1=(g'H)^{1/2}$ the velocity of the first baroclinic mode. The terms ϕ and $\boldsymbol{A}$ are commonly referred to as the scalar and vector potential, respectively. Note that the vector $\boldsymbol{\tau}/(c_1^2\cdot\rho)$ is dimensionless, and will be referred to as DWS in the following. Note also that ϕ and $\boldsymbol{A}$ have dimensions of length. Furthermore, note that since the DWS lies in the x-y plane, $\boldsymbol{A}=(0,0,S)$. The function S, is typically referred to as the DWS stream-function.

Using the Helmholtz decomposition of the DWS and the definitions above, the linear shallow water equation can be written in terms of ϕ and S as

$$\begin{cases}\dfrac{1}{g'}\left(\dfrac{\partial u}{\partial t}-fv\right)=\dfrac{\partial h}{\partial x}+\dfrac{\partial\phi}{\partial x}+\dfrac{\partial S}{\partial y}\\[2ex]\dfrac{1}{g'}\left(\dfrac{\partial v}{\partial t}+fu\right)=\dfrac{\partial h}{\partial y}+\dfrac{\partial\phi}{\partial y}-\dfrac{\partial S}{\partial x}\\[2ex]-\dfrac{\partial h}{\partial t}+D\left(\dfrac{\partial u}{\partial x}+\dfrac{\partial v}{\partial y}\right)=0\end{cases} \tag{8}$$

where D is a reference depth set to 120 m, h is the departure of the interface layer from D (i.e. $H=D-h$) and the continuity equation has been linearized around D as in Jin (1997). Jin (1997) sought for solutions of the quasi-geostrophic equations, in which h is in equilibrium with the zonal wind stress, and assumed the meridional wind stress to be zero. Here we seek for solutions of (8) around the interface layer computed by setting the ocean at the hydrostatic state (i.e. $u=v=0$). It is important to note that at this state, the zonal and meridional components of the DWS are in equilibrium with the zonal and meridional derivatives of the interface layer. We denote this interface as h_{eq}, and we will refer to this layer to as quasi-equilibrium layer. The momentum equations in (8) at the hydrostatic state are $\nabla h_{eq} + \nabla\phi + \nabla\times\mathbf{A}=0$, where we have used the definition (7) of scalar and vector potential. By extracting the divergence of this equation, we get $-\nabla^2 h_{eq}= \nabla^2\phi$. It is therefore natural to set $-h_{eq}=\phi$. This means that the divergence of the DWS, forces the "equilibrium" part of the dynamics. We indicate with $-q$ the displacement of the interface layer from its shape at the equilibrium state (h_{eq}), namely $h(x,y,t)=h_{eq}(x,y,t)-q(x,y,t)$. The DWS was decomposed in to irrotational and solenoidal components using the Helmholtz decomposition. The irrotational component (i.e. ϕ) was used to represent $-h_{eq}$.

In Figure 2a, the meridional mean of the h_{eq} anomaly is shown in relation to El Niño (indicated by the dots on the right vertical axis) and La Niña (indicated by the squares on the left vertical axis) events. It is evident that the deformation of the interface layer induced by h_{eq} is consistent with both El Niño and La Niña events.

In Figure 2b, we present the N_{34} obtained from equation (1) using the h_{eq} anomaly instead of the Z_{15} anomaly and the transfer function of Figure 1b. The correlation coefficient between the measured N_{34} and N_{34} reconstructed from the quasi-equilibrium dynamics (h_{eq}) is high (0.83), indicating that the quasi-equilibrium dynamics accurately capture the main features of the N_{34} variability. However, upon closer examination of Figure 2b, it is evident that the N_{34} deduced from the quasi-equilibrium dynamics underestimates N_{34} values during some strong (1965-66, 1972-73) and all extreme (1982-83, 1997-98, 2015-2016) El Niño events. As shown in Figure 2b (red and magenta bullets on the bottom axis), successive strong or extreme El Niño events occur over time scales longer than the interannual, suggesting that while the equilibrium dynamic accurately captures the interannual variability of SST anomalies in the central tropical Pacific, it only partially resolves the fluctuations of the N_{34} over longer time scales. This leads us to hypothesize that q, which is forced by the rotational part of the DWS, encapsulates the long-term variability of the Z_{15} anomaly and, thus, of the N_{34}. From equation (8), it is possible to derive an equation for q. However, a great simplification can be made by using the geostrophic approximation. A reasonable strategy to use this approximation is to exclude the equatorial belt between 2°S-2°N and derive an equation for q in the two strips between 2°N-20°N and 2°S-20°S. The geostrophic approximation appears reasonable because we are interested in the long-term, basin-scale variability of q. Using this approximation we find

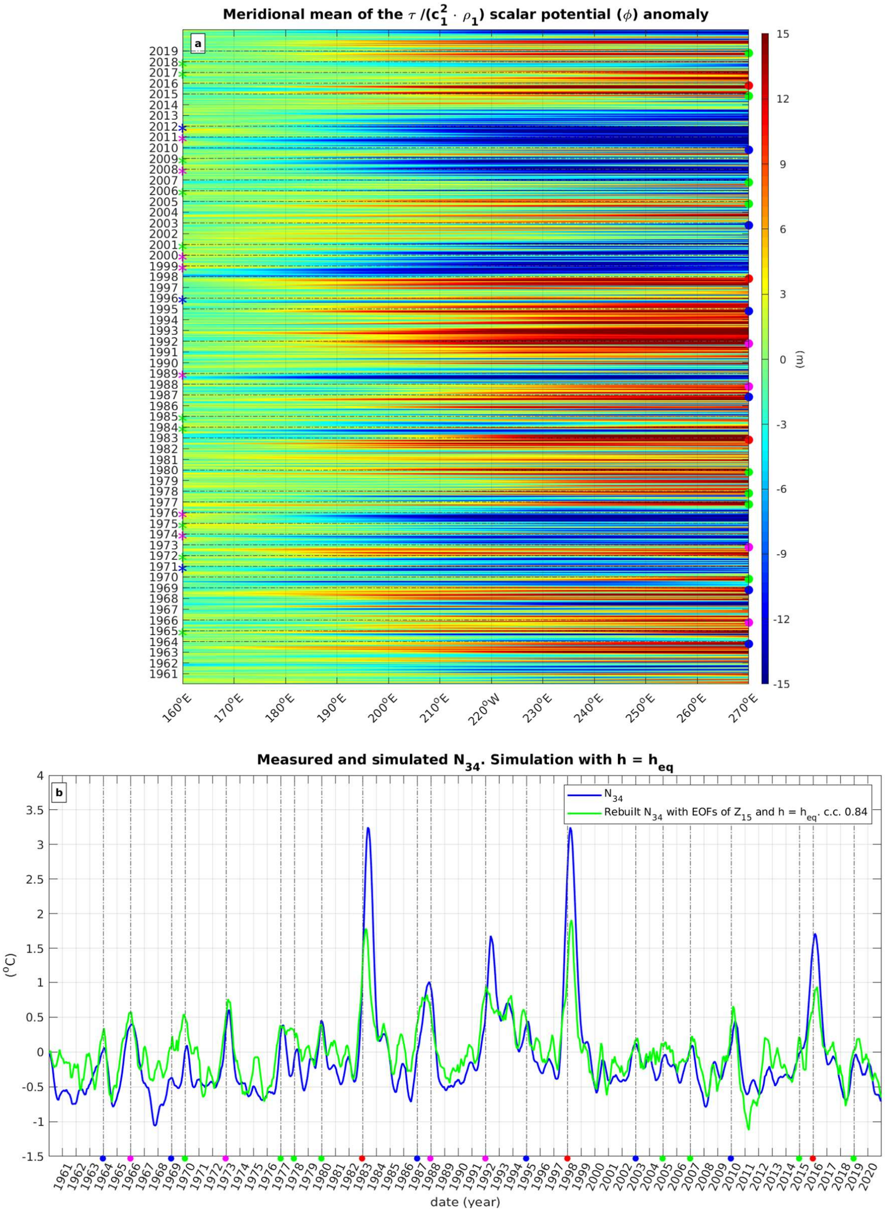

Figure 2: a) Meridional mean of the dimensionless wind stress potential anomaly. Colored dots on the right vertical axis represent El Niño events classified as discussed in the legend of Figure 1a. Colored rectangles on the left vertical axis represent La Niña events obtained from https://ggweather.com/enso/oni.htm, with the following legend: magenta, strong; blue, moderate; green, weak. b) Measured (blue line) and rebuilt N_{34} (green line) obtained with the transfer function of Figure 1b and substituting, in place of the Z_{15} anomaly, the anomaly of h_{eq}. Colored dots on the horizontal bottom axis represent El Niño events classified as discussed in the legend of Figure 1a.

$$\begin{cases} v = -\left(\dfrac{g'}{f}\right) \cdot \left(\dfrac{\partial S}{\partial y} - \dfrac{\partial q}{\partial x}\right) \\ u = -\left(\dfrac{g'}{f}\right) \cdot \left(\dfrac{\partial S}{\partial x} + \dfrac{\partial q}{\partial y}\right) \end{cases} \tag{9}$$

and, observing that $\partial h_{eq}/\partial t \approx 0$, substituting equation (9) in the continuity equation, we get

$$\frac{\partial q}{\partial t} - D\left(\frac{g' \cdot \beta}{f^2}\right) \cdot \frac{\partial q}{\partial x} = D\left(\frac{g'}{f}\right)\nabla^2 S - D\left(\frac{g' \cdot \beta}{f^2}\right)\frac{\partial S}{\partial y} \tag{10}$$

where $\beta = df/dy$.

To account for the slowly changing background mean climate conditions of the equatorial Pacific, we have considered $g' = g'(t)$, with $g'(t)$ representing the average spatial reduced gravity field over the region 20°S-20°N, 160°E-270°W. This was computed from TS data, as discussed in Appendix B. Figure 3 shows $g'(t)$ and illustrates that the reduced gravity field in the entire tropical Pacific is characterized by a trend of increase of approximately $0.33 \cdot 10^{-4}$ m/s^2 per year, in addition to oscillations over the sub-decadal time-scale. This increase in reduced gravity is a result of an increase in the stability of the water column, which is consistent with an increase of the stratification of the water column due to the uneven increase in temperature of the surface and bottom layers (An et al. 2008).

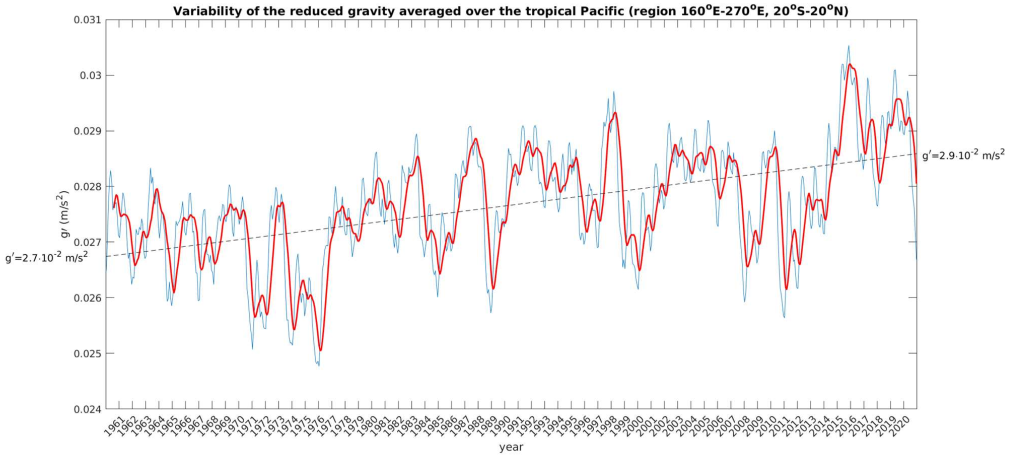

Figure 3: Spatial average of the reduced gravity field over the region 20°S-20°N, 160°E-270°E. The blue line represents raw data; the red line represents 5-month median filtered data; the black dashed line is the linear fit.

https://doi.org/10.5194/egusphere-2026-2393
Preprint. Discussion started: 28 May 2026

With the above observation, equation (10) describes an internal wave (*q*-wave in the following) forced by the rotational component of the DWS that propagates westward over the equilibrium thermocline (i.e. h_{eq}) with a velocity $c = D\cdot(g'\cdot\beta/f^2)$ that depends on time and latitude.

Figure 4a displays the time-averaged spatial distribution of the DWS streamline function (*S*) anomaly, while Figure 4b depicts the temporal variability of the space-averaged *S* anomaly. In the western part of the basin, the *S* anomaly is characterized by a positive-value region south of the equator and a negative-valued region north of it. In contrast, the eastern tropical Pacific shows two regions with positive values both south and north of the equator. The spatial pattern of the *S* anomaly in the western tropical Pacific is consistent with mass redistribution towards the equator due to Sverdrup transport. However, in the eastern part of the basin, the spatial structure of the *S* anomaly is consistent with Sverdrup transport towards the equator in the south and Sverdrup transport away from the equator in the north. This suggests that in the eastern tropical Pacific, wind stress curl is not as effective in transporting mass towards the equator as it is in the western part of the basin. This asymmetry could be related to ENSO asymmetry, but further, focused research is necessary to clarify this issue. The temporal variability of the spatially averaged *S* anomaly (Figure 4b, green line) does not appear to be dominated by specific frequencies. However, the residual signal obtained after applying a low-pass filter with a cut-off frequency of 10^{-1} years^{-1} (Figure 4b, red line) is weak, suggesting that the S anomaly is only minimally affected by interdecadal variability.

The *q*-wave field was calculated separately for the northern and southern regions of the equator by solving equation (10) with an initial condition of zero, using the technique outlined in Appendix C. In order to provide the reader with a better understanding of the spatial and temporal variability of the *q*-wave field, the *q*-wave time series was decomposed into EOFs. The *q*-wave field is primarily described by two EOF modes, which together explain 98% of the variance. Figure 5a displays the first EOF of the *q*-wave field, while Figure 5b shows its corresponding PC. Similarly, Figure 5c and 5d depict EOF2 and its corresponding PC, respectively. Both EOFs demonstrate that the *q*-wave field is primarily concentrated in the subtropical region between 2^{o}S-7^{o}S and 2^{o}N-7^{o}N. Along the zonal direction, EOF1 describes two negative patterns located in the western and eastern parts of the basin, and another region of positive values that fills the entire central part of the tropical Pacific. The corresponding PC1, describes a linear trend which transits from negative to positive values by the beginning of 1990. This implies that, from 1960 to 1990, *q*-waves contributed to the rise (note that $h = h_{eq}$-q) of the thermocline from its equilibrium position, while in the subsequent period they contributed to the deepening of the thermocline in these regions. Conversely, in the central tropical Pacific during 1960-1990, *q*-waves contributed to the deepening of the thermocline and the rise of it in the period 1990-2020.

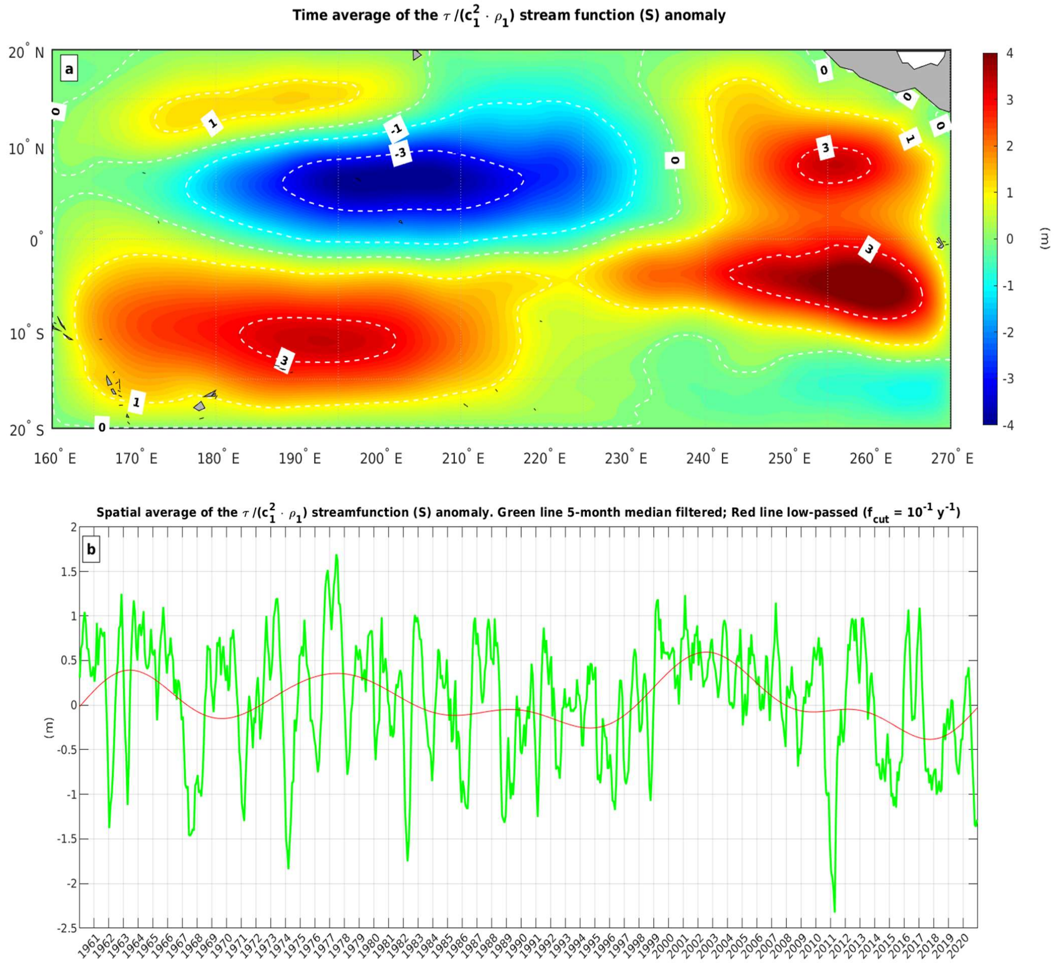

Figure 4: a) Time average of the dimensionless wind stress stream-function anomaly. b) Spatial average over the region 20ºS-20ºN, 160ºE-270ºE of the dimensionless wind stress stream-function anomaly.

In the zonal direction, EOF2 is characterized by three distinct regions: two with positive values in the western and central parts of the basin, and one with negative values in the eastern tropical Pacific. The temporal variability of this spatial pattern is represented by PC2, as shown in Figure 5d. A visual inspection of Figure 5d reveals that PC2 of the q-wave field is characterized by a strong long-term variability, with a weak interannual variability.

https://doi.org/10.5194/egusphere-2026-2393
Preprint. Discussion started: 28 May 2026

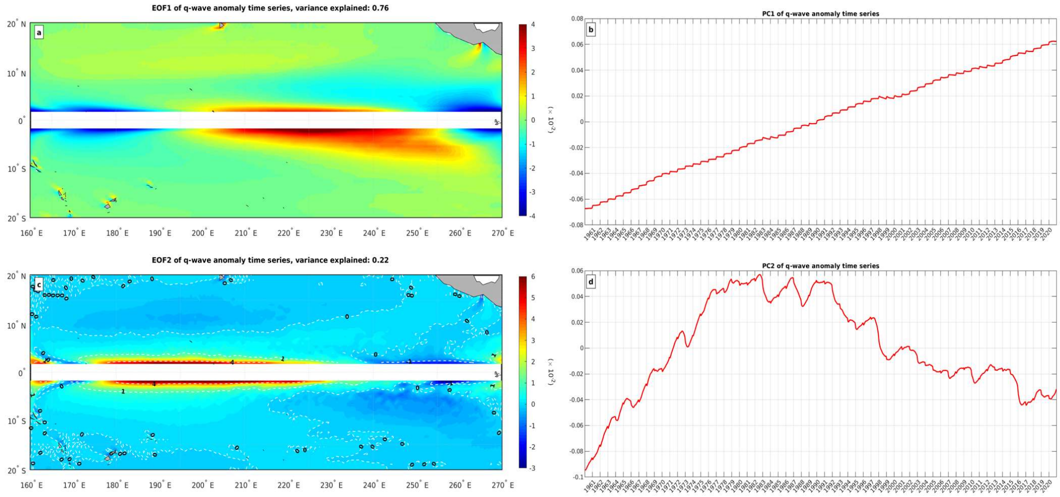

Figure 5: EOF analysis of the q-wave anomaly field obtained with initial condition $q_0 = 0$. a) EOF1. b) PC1. c) EOF2. d) PC2.

To analyze the effect of q-wave interdecadal variability on SST anomalies in the central tropical Pacific, we reconstructed the N_{34} using equation (1) and replacing the Z_{15} anomaly with the h_{eq}-q anomaly, with q computed with the initial condition set to zero. The results are shown in Figure 6, where we have plotted, beside the estimate of N_{34} obtained by replacing the Z_{15} anomaly with h_{eq}-q anomaly, the measured N_{34} (blue line) and the estimated N_{34} using the h_{eq} anomaly (green line, same as Figure 2a) for comparison. It is evident that the inclusion of the q-wave significantly improves the accuracy of the N_{34} estimate. In particular, the addition of the q-wave allows for a more precise representation of strong and extreme El Niño events, compared to using only h_{eq}.

To demonstrate that the improvement in the N_{34} estimate is a result of low frequency signals encapsulated in q, which are filtered out by the "quasi-equilibrium" assumption, in Figure 6 we have also plotted the N_{34} estimate obtained by replacing the Z_{15} anomaly with the residual signal of the h_{eq} minus the low-passed q (represented by a black dashed line). The low pass filtering was performed with a frequency cut of 10^{-1} years^{-1}. It can be observed that the low-pass filtering of q results in a N_{34} estimate that is similar to that obtained using the unfiltered q-signal (compare the red land black dashed line). This demonstrates that the interannual variability of the SST anomaly in the central tropical Pacific can be explained by the equilibrium dynamics, which encapsulates the variability of the interface layer over time scales shorter than 10 years, and is associated with the divergence of the DWS. On the other hand, q-waves are responsible for the long-term variability of SST anomalies, as they reflect the non-equilibrium dynamics of the thermocline. These waves are driven by the rotational component of the DWS. Mathematically, they represent deviations of the thermocline from its shape at the hydrostatic state, caused by the curl of the DWS. Physically, q-waves are a result of the thermocline accommodation due to mass redistribution caused by the Sverdrup transport. As mass in the surface layer is displaced meridionally by the Sverdrup transport, the thermocline responds by generating q-waves that propagate zonally.

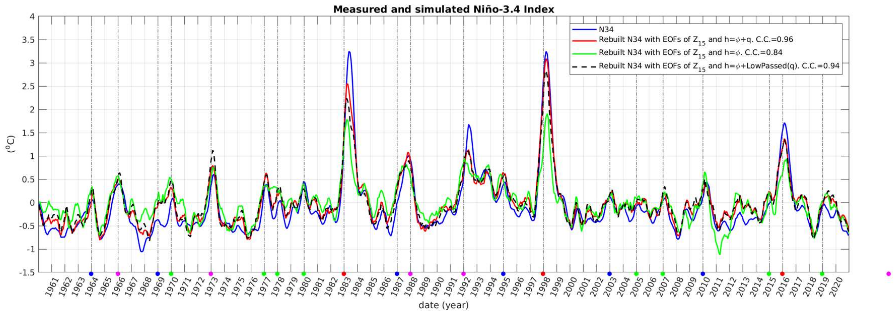

Figure 6: Measured (blue solid line) and simulated N_{34}. Red solid line: N_{34} simulated using the transfer function of Figure 1b and substituting, in place of the Z_{15} anomaly, the anomaly of the interface layer computed as $h = h_{eq} - q$. Green line: N_{34} simulated using the transfer function of Figure 1b and substituting, in place of the Z_{15} anomaly, the anomaly of the interface layer computed as $h = h_{eq}$ (same as green line of Figure 2). Black dashed line: N_{34} obtained from low passed q. Colored dots on the horizontal bottom axis represent El Niño events classified as discussed in the legend of Figure 1a.

5. Discussion and Conclusion

In this study, we have investigated the relationships between the thermocline depth anomaly, and wind stress in the entire tropical Pacific, and changes in the average SST anomaly in the central part of the basin over both interannual and interdecadal time scales. Our results indicate that the variability in the SST anomaly in the central tropical Pacific can be accurately represented by an integral relationship, which links the variability in the thermocline depth anomaly to the Niño-3.4 index. This integral relationship is defined by a transfer function derived from an EOF analysis of the thermocline depth anomaly, which we have assumed to be represented by the 15° isotherm depth anomaly. The spatial structure of the transfer function indicates that even small variations in the thermocline depth anomaly in the western or eastern parts of the tropical Pacific can have significant impacts on the SST anomaly in the central part of the basin, while large variations in the thermocline depth anomaly in the central Pacific have minimal influence on SST variation in this region. This result is consistent with Zhong et al. (2025), who demonstrated, using a different approach, that El Niño is more predictable in the eastern and western parts of the tropical Pacific compared to the central part of the basin.

https://doi.org/10.5194/egusphere-2026-2393
Preprint. Discussion started: 28 May 2026

Our analysis has shown that the transfer function's structure remains stable regardless of the chosen period for EOF analysis of the thermocline depth anomaly. However, the effectiveness of the transfer function in capturing the interdecadal variability of the N_{34} may vary depending on the specific period selected for the EOF analysis. To definitively address this issue, a systematic sensitivity test would be necessary. We have only performed a few spread tests, which suggest that in order to accurately capture the long-term variability of the N_{34} in relation to changes in the thermocline depth anomaly, the EOF analysis of the thermocline depth anomaly must be conducted over a sufficiently long period to include a range of El Niño and La Niña events with varying intensities. This is evident in the period 1960-1990, which includes 11 El Niño events (four weak, three moderate, three strong, and one extreme) and 14 La Niña events (eight weak, one moderate, and five strong).

To analyze the impact of wind stress variability on SST anomalies in the central tropical Pacific, we examined the coupling between changes in the depth of the thermocline and the irrotational (curl-free) and solenoidal (divergence-free) components of the DWS. The use of the DWS is necessary because, even a wind stress without divergence or curl, can provide divergence or vorticity to the horizontal ocean dynamics through spatial changes of the first baroclinic mode velocity and/or surface density. Our findings indicate that the irrotational component of the DWS, which is related to the divergence of the DWS and drives the quasi-equilibrium dynamics, is the main factor influencing the interannual variability of SST anomalies in the central tropical Pacific. This is consistent with the findings of Eusebi Borzelli and Carniel (2023), who observed that the region of maximum wind convergence in the tropical Pacific shifts along the zonal direction in phase with the SOI. This suggests that the divergence of the wind field can explain the variability of the tropical Pacific climate system on the ENSO time-scale.

In this research, we have demonstrated that the equilibrium dynamics can be described by an equation between the DWS scalar potential and the deformation of the interface layer. This equation takes the form $-\nabla^2 h_{eq} = \nabla^2 \phi$ and we have set $-h_{eq} = \phi$. Although the most natural, this solution is not the most general and this choice could be questioned. A more general solution could be, for instance, $-h_{eq} = \phi+\alpha \cdot x+\beta \cdot y$, where the linear components represent the average slope over the entire observation period of the thermocline in the zonal and meridional directions. However, this signal does not contribute to the h_{eq} anomaly, and for the sake of simplifying the formalism, we have chosen to set $h_{eq} = -\phi$.

Non-equilibrium dynamics associated with the solenoidal component of the DWS, which represents its rotational contribution, becomes important on timescales longer than a decade. This solenoidal component drives the generation of internal waves, referred to as q-waves, which propagate westward and induce large-scale deformations of the thermocline. In physical terms, q-waves describe the thermocline response to Sverdrup transport due to wind stress curl. Figure 7 shows schematically the

https://doi.org/10.5194/egusphere-2026-2393
Preprint. Discussion started: 28 May 2026

generation process of *q*-waves. It should be noted that the propagation speed of *q*-waves is formally similar to that of long, off-equatorial, internal Rossby waves. Therefore, *q*-waves can be classified as Rossby-like waves. However, there are some notable differences between the two. Specifically, Rossby waves travel over a flat thermocline, while *q*-waves are caused by the rotational (solenoidal) component of wind stress and result in a deviation of the thermocline from its shape at hydrostatic equilibrium. As a result, *q*-waves propagate over a more complexly shaped thermocline. Furthermore, unlike ordinary Rossby waves, the propagation speed of *q*-waves depends explicitly on time due to the temporal variability of reduced gravity.

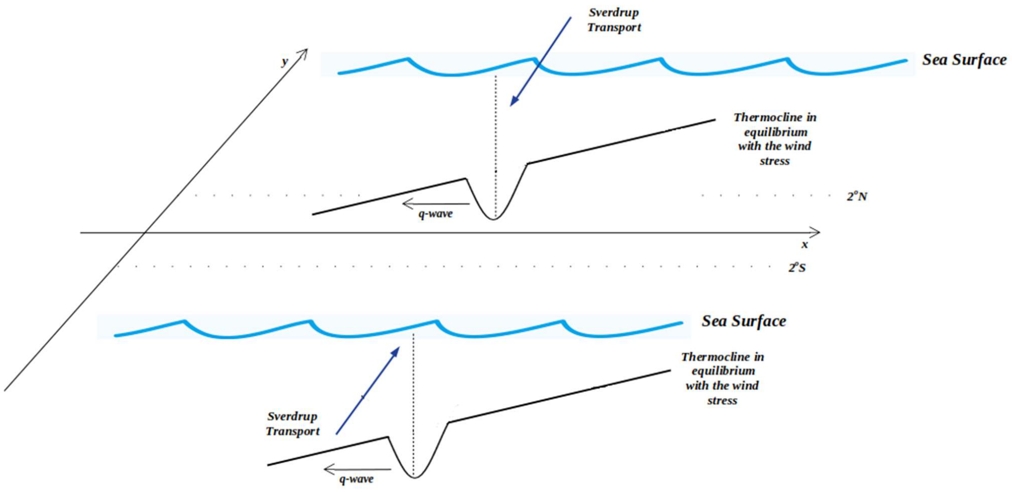

Figure 7: Schematical representation of *q*-waves.

By modulating thermocline depth, *q*-waves contribute to SST anomaly variability in the central tropical Pacific and provide a dynamical pathway through which non-equilibrium ocean processes influence surface temperature. Although the solenoidal component of the DWS itself exhibits limited variability on interdecadal time scales, it acts on a background ocean state whose stratification evolves slowly over time. Such long-term changes in stratification are captured by variations in the reduced gravity field (g'), which reflects uneven temperature changes between the upper and lower ocean layers.

Our results indicate that interdecadal variability of SST anomalies in the central tropical Pacific arises from the coupling between the slowly varying reduced gravity field and the solenoidal component of the DWS. In this framework, changes in surface ocean density modulate the efficiency of Sverdrup transport associated with wind stress curl, thereby controlling the long-term thermocline response and its imprint on SST variability. This mechanism complements the equilibrium dynamics dominant at interannual timescales and highlights the role of rotational wind forcing in shaping the long-term ENSO variability.

The uneven heating of the surface and bottom layers of the tropical Pacific under greenhouse warming described by An et al. (2008) has the obvious consequence of increasing the stability of the water column and, therefore, increasing the reduced gravity. However, the role of surface salinity in determining changes in the reduced gravity field is less certain, although some authors have emphasized the importance of including sea surface salinity records to improve El Niño forecasting (e.g. Wang et al., 2024). In addition to the redistribution of salt by ocean currents, the acceleration of the hydrological cycle under greenhouse warming also contributes to regional means and long-term trends in sea surface salinity (Durack et al., 2012). However, it has been shown that estimates of long-term trends in sea surface salinity in the tropical Pacific are regionally dependent (Zhi et al., 2025). While our research did not specifically address the impact of long-term surface salinity trends on the variability of the reduced gravity field, a focused analysis using the methods presented here could provide insight into the role of salinity changes in the interdecadal variability of SST anomalies in the tropical Pacific.

As a final remark, some authors have noted that the 2023-24 El Niño event was unusual due to its significant oceanic warming, but relatively subdued Southern Oscillation and wind anomalies over the tropical Pacific (Pang et al., 2025). This suggests that the event was not influenced by the traditional Bjerknes feedback mechanism. According to these authors, the intense oceanic warming was mainly caused by the accumulation of heat content in the western Pacific during the preceding prolonged La Niña period, and they attributed the event to oceanic processes. In the terminology of this research, an increased heat piled up in the western tropical Pacific is expected to contribute to increasing the stability of the water column and, in turn, increase the reduced gravity. According to Pang et al. (2025), the 2023-24 El Niño was dominated by interannual variability and the geostrophic approximation used here is only able to capture variability over a time-scale longer than 3-4 years. However, it is interesting to note that, according to equation (10), an increased reduced gravity determines a more efficient forcing of q-waves by the rotational component of the dimensionless wind stress. In order to clarify this issue, more specific approximations that allow for the derivation of an equation capable of capturing the interannual variability of *q*-waves, based on, for instance, the quasi-geostrophic approximation used in Jin (1997), are necessary.

Appendix A: solution of equation (3) and derivation of equation (5)

We have used dimensionless EOF analysis of the Z_{15} anomaly. This EOF algorithm is summarized by the following equations

$$\begin{aligned}\boldsymbol{Z}(t) &= \sum_{m=1}^{M} \sqrt{\lambda_m}\,\alpha_m(t)\cdot \boldsymbol{Y}_m(x_i)\\ \alpha_n(t_j) &= \frac{1}{\sqrt{\lambda_n}}[\boldsymbol{Z}(t)]^T \cdot \boldsymbol{Y}_n(x_m)\end{aligned} \tag{A.1}$$

that, for convenience we have rewritten in vector form defining the column vectors $\boldsymbol{Z}(t)$, whose i^{th} element is $Z(x_i,t)$ $(i=1...M)$, and $\mathbf{Y}_m$, whose i^{th} element is the value of the m^{th} $(m=1...M)$ EOF at point x_i. In equation (A.1), the suffix T indicates the transpose. After rewriting equation (3) in matrix form, observing that $\mathbf{Y}_k$ are eigenvectors of $\mathbf{A}$, with an obvious notation, expressing $\boldsymbol{w}=q_1\boldsymbol{Y}_1+...+q_M\boldsymbol{Y}_M$ and $\boldsymbol{n}=b_1\boldsymbol{Y}_1+...+b_M\boldsymbol{Y}_M$ we have $q_k = b_k/\lambda_k$, where b_k is the projection of $\boldsymbol{n}$ along the direction of the k^{th} EOF, i.e. $b_k = \boldsymbol{n}^T\cdot\mathbf{Y}_k$. Therefore, $b_k = \boldsymbol{n}^T \cdot \boldsymbol{Y}_k = \int_0^T \frac{dt}{T} N_{34}(t)\cdot[\boldsymbol{Z}(t)]^T\cdot\boldsymbol{Y}_k = \sqrt{\lambda_k}\int_0^T\frac{dt}{T}N_{34}(t)\cdot\alpha_k(t)$or

$$\boldsymbol{w} = \sum_{n=1}^{M}\frac{\boldsymbol{Y}_n}{\sqrt{\lambda_n}}\cdot\int_0^T\frac{dt}{T}N_{34}(t)\cdot\alpha_n(t) \tag{A.2}$$

which is equation (5).

Appendix B: determination of the reduced gravity field and first baroclinic mode velocity

To compute the reduced gravity and the velocity of the first baroclinic mode we used the strategy suggested by Eusebi Borzelli and Carniel (2023) and Eusebi Borzelli et al. (2024). Firstly, the ocean's vertical structure was assumed to consist of two layers, and the density profiles were fitted with a step function. This involved dividing each profile into two sub-segments of varying length and calculating the average density for each segment. The resulting step function representations were then compared to the original profile, and the one with the lowest root-mean-square was selected as the best step function representation of the water column. This process was repeated for each date of the observation period, providing spatial distributions of density in the surface ($\rho(x,y,t)$) and bottom ($r(x,y,t)$) layers and a "first approximation" depth of the surface layer ($H^0(x,y,t)$). In the calculation of the velocity of the first baroclinic mode, we excluded all points in which $H^0(x,y,t)$ was less deep than 60 m (with 60 m supposed to be the maximum depth of the mixed layer) and $\rho(x,y,t) \geq r(x,y,t)$. This was done to avoid spurious results due to density changes in the mixed layer and instabilities in the water column. The velocity of the first baroclinic mode was obtained by solving the vertical mode equation (Wusch and Stammer, 1997), namely

$$\frac{d}{dz}\left[\frac{1}{N^2(x,y,z,t)}\cdot\frac{dP_n}{dz}\right]+\frac{1}{c^2{}_n(x,y,t)}P_n=0 \tag{B.1}$$

subject to rigid upper and lower boundary conditions, at each date of the observation period, in each point of the observation domain. In equation (B.1), $N^2(x,y,z,t)$ is the buoyancy frequency, $n=0,1\ldots$, with $n=0$ indicating the barotropic mode, and $1/c^2n$ are real-valued, positive eigenvalues, with cn indicating the velocity of the nth baroclinic mode. In the final calculation of the depth of the surface layer, we excluded all points in which $H^0(x,y,t)$ was less deep than 60 m (with 60 m supposed to be the maximum depth of the mixed layer) and $\rho(x,y,t) \geq r(x,y,t)$. This was done to avoid spurious results due to density changes in the mixed layer and instabilities in the water column. **Appendix C: Solution of equation (10).**

Equation (1) was transformed in to a system of ordinary independent differential equations using the Fourier method. Observing that in equation (10) the latitude is a parameter, at every latitude it can be rewritten as

$$\frac{\partial q}{\partial t}-c_y(t)\cdot\frac{\partial q}{\partial x}=b_y(x,t)\text{where}\begin{cases} c_y(t)=D\left(\frac{g\prime\cdot\beta}{f^2}\right)\\ b_y(x,t)=D\left(\frac{g\prime}{f}\right)\nabla^2 S-D\left(\frac{g\prime\cdot\beta}{f^2}\right)\frac{\partial S}{\partial y}\end{cases} \tag{C.1}$$

Fixing the latitude, indicating with $Q(k,t)$ and $B(k,t)$ the Fourier transforms along the zonal directions of $q(x,t)$ and $b_y(x,t)$, we get a system of decoupled ordinary differential equation of the form

$$\frac{dQ}{dt}-ik\cdot c_y(t)Q=B(k,t)\text{with initial condition } Q(k,t=0)=Q_0(k) \tag{C.2}$$

where $Q_0(k)$ is the Fourier transform of the initial condition $q(x,t=0) = q_0(x)$.

We solved equation (C.2) using the integrating factor. Namely, setting$\mu(t)=exp\left[-ik\int_0^t c_y(s)\cdot ds\right]$we have

$$Q(k,t)=\frac{Q_0(k)+\int_0^t ds\, B(k,s)\cdot\mu(s)}{\mu(t)} \tag{C.3}$$

Code availability

Matlab scripts, developed for this research under Matlab release 2018a, can be downloaded at https://doi.org/10.6084/m9.figshare.30609104

https://doi.org/10.5194/egusphere-2026-2393
Preprint. Discussion started: 28 May 2026

Data availability

Data used in this research can be downloaded succumbing to European Union (EU) regulations on geophysical data exchange (see https://www.copernicus.eu/en/international-cooperation-area-data-exchange).

Original ERA5 wind and SST data can be downloaded from the Copernicus data archive by registered users at

https://cds.climate.copernicus.eu/datasets/reanalysis-era5-single-levels-monthly-means?tab=overview

Original monthly T-S data were made available by the Institute of Atmospheric Physics (IAP) of the Chinese Academy of Sciences (CAS) and can be downloaded the at the following web site

http://www.ocean.iap.ac.cn/pages/dataService/dataService.html?navAnchor=dataService

Authors' contributions

All the authors contributed equally to the work. G.L.E.B. and S.C. proposed the original idea and designed the research. All authors contributed to analyze the data and to interpret the results. G.L.E.B. and C.E.C. provided the figures. G.L.E.B. wrote the initial version of the manuscript, S.C., C.E.C. and M.S. provided corrections and comments.

Competing Interests

The authors declare no competing interest.

Acknowledgements

Prof. Wenxiu Zhong is greatly acknowledged for the discussions and suggestions during the initial phase of the research.

Funding

This research received no funding

References

An, S.-I., Kug, J.-S., Ham, Y.-G., Kang, I.-S.: Successive modulation of ENSO to the future greenhouse warming. J. Clim., 21, 3–21, doi: https://doi.org/10.1175/2007JCLI1500.1, 2008

Bjerknes, J.: Atmospheric teleconnections from the equatorial Pacific, Mon. Wea. Rev., 97, 163–172, 1969

Burgers, G., Jin, F.-F., van Oldenborgh, G. J.: The simplest ENSO recharge oscillator, Geophys. Res. Lett., 32, L13706, doi: https:/doi.org/10.1029/2005GL022951, 2005

Cai, W. et al.: ENSO and greenhouse warming, Nat. Clim. Change, 5, 849–859, doi: https:/doi.org/10.1038/NCLIMATE2743, 2015

Cai, W. et al.: Changing El Niño–Southern Oscillation in a warming climate, Nature Reviews Earth & Environment, 2(9), 628-644, doi: https:/doi.org/10.1038/s43017-021-00199-z, 2022

Collins, M. et al.: The impact of global warming on the tropical Pacific Ocean and El Niño, Nat. Geosci., 3, 391–397, doi: https:/doi.org/10.1038/ngeo868, 2010

Cane, M. A., Zebiak, S.: A Theory for El Niño and the Southern Oscillation, Science, 228, 4703, 1085-1087, doi: https:/doi.org/10.1126/science.228.4703.108, 1985

Capotondi, A., and P. D. Sardeshmukh, P. D.: Optimal precursors of different types of ENSO events, Geophys. Res. Lett., 42, 9952–9960, doi: https:/doi.org/10.1002/2015GL066171, 2015

Capotondi, A., Ricciardulli, L.: The influence of pacific winds on ENSO diversity, Sci. Rep., 11, 18672. doi: https:/doi.org/10.1038/s41598-021-97963-4, 2021

Carrillo, C. N.: Desertacion sobre las corrientes y estudios de la corriente Peruana de Humboldt, Bol. Soc. Geogr. Lima, 11, 72–110, 1892

Cheng L., Trenberth, K., Fasullo, J., Boyer, T., Abraham, J., Zhu, J. : Improved estimates of ocean heat content from 1960 to 2015, Science Advances, 3, e1601545, doi: https:/doi.org/10.1126/sciadv.1601545, 2017

Durack, P. J., Wijffels, S. E., Matear, R. J.: Ocean salinities reveal strong global water cycle intensification during 1950 to 2000, Science, 336(6080), 455–458. doi: https:/doi.org/10.1126/science.1212222, 2012

Eusebi Borzelli, G. L., Carniel, S.: Where the winds clash: what is really triggering El Niño initiation?, npj Clim. Atmos. Sci., 6, 119, doi: https:/doi.org/10.1038/s41612-023-00445-9, 2023

Eusebi Borzelli, G. L., Napolitano, E., Carillo, A., Struglia, M.V., Palma, M. and Iacono, R.: Hydrographic vs. Dynamic Description of a Basin: The Example of Baroclinic Motion in the Ionian Sea, MDPI-Oceans, 5, 2, 383-397, doi: https:/doi.org/10.3390/oceans5020023, 2024

Fedorov, A. V., Philander, S. G.: A stability analysis of tropical ocean-atmosphere interactions: Bridging measurements and theory for El Niño, J. Clim., 14, 3086–3101. doi: https:/doi.org/10.1175/1520-0442(2001)014<3086:ASAOTO>2.0.CO;2, 2001

Graham, N. E.: Decadal-scale climate variability in the 1970s and 1980s: Observations and model results. Climate Dyn., 10, 135–162. doi: https:/doi.org/10.1007/BF00210626, 1994

Hu, S., Fedorov, A. V.: Cross-equatorial winds control El Niño diversity and change, Nat. Climate Change, 8, 798–802, doi: https:/doi.org/10.1038/s41558-018-0248-0, 2018

Jiang, N., Neelin, J. D., Ghil, M.: Quasi-quadrennial and quasi-biennial variability in the equatorial Pacific, Climate Dynamics, 12, 101–112, doi: https:/doi.org/10.1007/BF00223723, 1995

Jin, F. F.: An equatorial ocean recharge paradigm for ENSO. Part I: conceptual model, J. Atmos. Sci., **54**, 811–829, doi: https:/doi.org/10.1175/1520-0469(1997)054<0811:AEORPF>2.0.CO;2, 1997

Jin, F.-F., Kim S. T., Bejarano, L.: A coupled-stability index for ENSO, Geophys. Res. Lett., 33, L23708, doi: https:/doi.org/10.1029/2006GL027221, 2006

Large, W. G., and Pond, S.: Open ocean momentum flux measurements in moderate to strong winds. Journal of physical oceanography, 11(3), 324-336. doi: https:/doi.org/10.1175/1520-0485(1981)011<0324:OOMFMI>2.0.CO;2, 1981

Liu, Z., Vavrus, S., He, F., Wen, N. & Zhong, Y.: Rethinking tropical ocean response to global warming: the enhanced equatorial warming, J. Clim. 18, 4684–4700, doi: https:/doi.org/10.1175/JCLI3579.1, 2005

Morse, P. M., Feshbach, H.: Methods of Theoretical Physics, McGraw-Hill, 1953

Newman, M., Sardeshmukh, P. D. Penland C.: How important is air-sea coupling in ENSO and MJO evolution, J. Clim., 22, 2958–2977, doi: https:/doi.org/10.1175/2008JCLI2659.1, 2009

Newman, M., Shin, S.-I., and M. A. Alexander M. A.: Natural variation in ENSO flavors, Geophys. Res. Lett., 38, L14705, doi: https:/doi.org/10.1029/2011GL047658, 2011

Peng, Q., S.-P. Xie, D. Wang, Y. Kamae, H. Zhang, S. Hu, X.-T., Zheng, Wang, W.: Eastern Pacific wind effect on the evolution of El Niño: Implications for ENSO diversity, J. Climate, 33, 3197–3212, doi: https:/doi.org/10.1175/JCLI-D-19-0435.1, 2020

Peng, Q., Xie, S. P., Miyamoto, A., Deser, C., Zhang, P., Luongo, M. T.: Strong 2023–2024 El Niño generated by ocean dynamics, Nat. Geosci., 18, 471–478, doi: https:/doi.org/10.1038/s41561-025-01700-9, 2025

Penland, C., Sardeshmukh P. D.: The optimal growth of tropical sea surface temperature anomalies, J. Clim., 8, 1999–2024, doi: https:/doi.org/10.1175/1520-0442(1995)008<1999:TOGOTS>2.0.CO;2, 1995

Périgaud, C., Zebiak, S. E., Mélin, F., Boulanger, J.-P., and Dewitte, B.: On the role of meridional wind anomalies in a coupled model of ENSO, J. Climate, 10, 761–773, doi: https:/doi.org/10.1175/1520-0442(1997)010,0761:OTROMW.2.0.CO;2, 1997

Philander, S. G. H., Pacanowski, R. C.: The oceanic response to cross-equatorial winds (with application to coastal upwelling in low latitudes), Tellus, 33A, 201–210, doi: https:/doi.org/10.3402/tellusa.v33i2.10708, 1981

Philander, S. G.: El Niño, La Niña and the Southern Oscillation, Academic Press, New York, 289 pp., 1990

Picaut, J., Delcroix, T.: Equatorial wave sequence associated with warm pool displacements during the 1986-1989 El Niño-La Niña, J. Geophys. Res., **100**(C9), 18393-18408. doi: https:/doi.org/10.1029/95JC01358, 1995

Quinn, W. H., Neal, V.T.: Recent climate change and the 1982–83 El Niño, Proc. Eighth Annual Climate Diagnostic Workshop, Downsville, ON, Canada, NOAA, 148–154, 1984

Quinn, W. H., Neal, V.T.: Recent long-term climate change over the eastern tropical and subtropical Pacific and its ramifications, Proc. 9th Annual Climate Diagnostic Workshop, Corvallis, OR, NOAA, 101–109, 1985

Rasmusson, E. M., Wang, X., Ropelewski, C. F.: The biennial component of ENSO variability, J. Mar. Systems, 1, 71-96, doi: https:/doi.org/10.1017/0924-7693(90)90153-2, 1990

Santoso, A., Mcphaden, M. J., Cai,, W.:. The defining characteristics of ENSO extremes and the strong 2015/2016 El Niño, Rev. Geophys., **55**(4), 1079-1129. doi: https:/doi.org/10.1002/2017RG000560, 2017

Trenberth, K. E.: Recent observed interdecadal climate changes in the Northern Hemisphere, Bull. Amer. Meteor. Soc., 71, 988–993, 1990

Trenberth, K. E., and J. W. Hurrell, J. W.: Decadal atmospheric–ocean variations in the Pacific, Climate Dyn., 9, 303–309. doi: https:/doi.org/10.1007/BF00204745, 1994

Wang, C. and Fiedler, P.C.: ENSO Variability and the Eastern Tropical Pacific: A Review, Progress in Oceanography, 69, 239-266. doi: https:/doi.org/10.1016/j.pocean.2006.03.004, 2006

Wang, H., Zheng, X. T.: Interdecadal Variability of the Meridional Wind across the Eastern Equatorial Pacific and Its Relationship with ENSO, Journal of Climate, 36(12), 4189-4202, doi: https:/doi.org/10.1175/JCLI-D-22-0516.1, 2023

Wang, H., Hu, S., Guan, C., Li, X.: The role of sea surface salinity in ENSO forecasting in the 21st century, npj Clim. Atmos. Sci., 7, 206. doi: https:/doi.org/10.1038/s41612-024-00763-6, 2024

Wyrtki, K.: El Niño—The dynamic response of the equatorial Pacific Ocean to atmospheric forcing, J. Phys. Oceanogr., **5**, 572–584, 1975

Wusch, C., Stammer, D.: Atmospheric loading and the oceanic “inverted barometer” effect, Rev. Geophys., **35,** 1, 79-107, doi: https:/doi.org/10.1029/96RG03037, 1997

Xie, S.-P. et al.: Global warming pattern formation: Sea surface temperature and rainfall, Journal of Climate, 23, 966–986, doi: https:/doi.org/10.1175/2009JCLI3329.1, 2010

Xie, S. P., Peng, Q., Kamae, Y., Zheng, X. T., Tokinaga, H., Wang D.: Eastern Pacific ITCZ dipole and ENSO diversity, Journal of Climate, 31(11), 4449-4462, doi: https:/doi.org/10.1175/JCLI-D-17-0905.1, 2018

Zhong, W., Sullivan, A., Eusebi Borzelli, G.L., Li, Z.: Early signs of strong El Niño–Southern Oscillation episodes, Sci. Rep., 15, 17225, doi: https:/doi.org/10.1038/s41598-025-01809-2, 2025

Zhi, H., Zhang, RH., Dong, M., Wu, M.: Upper ocean salinity and temperature changes and their contributions to the stratification in the tropical Pacific under global warming, Clim. Dyn., 63, 93, doi: https:/doi.org/10.1007/s00382-024-07570-y, 2025